

MEASUREMENT AND MODELING OF Na-LIKE Fe xvi INNER-SHELL SATELLITES BETWEEN 14.5 Å AND 18 Å

A. GRAF¹, P. BEIERSDORFER², G. V. BROWN², AND M. F. GU²

¹ Physics Department, University of California-Davis, 1 Shields Avenue, Davis, CA 95616, USA

² University of California Lawrence Livermore National Laboratory, 7000 East Avenue, Livermore, CA 94550, USA

Received 2007 September 12; accepted 2009 January 13; published 2009 April 3

ABSTRACT

We have used the University of California Lawrence Livermore National Laboratory’s EBIT-I electron beam ion trap to perform measurements of the wavelengths and relative intensities of the X-ray lines from inner-shell satellite transitions in sodium-like Fe xvi. The measurements were carried out with high-resolution crystal and grating spectrometers and covered the 14.5–18 Å wavelength band. In contrast to some predicted line strengths and positions found in the literature, our results show that the strongest relatively unblended inner-shell satellites of Fe xvi are located near 15.2 Å. This is near the location of the $3d \rightarrow 2p$ intercombination line in Fe xvii. Calculations using the Flexible Atomic Code (FAC) are presented. The average deviation between the EBIT-I measurements and the FAC calculations for the wavelength positions and line ratios are 22 mÅ and a factor of 2.3, respectively, where the average is taken over the ten features included in this work.

Key words: line: identification – X-rays: general

Online-only material: color figures

1. INTRODUCTION

In a multitude of astrophysical X-ray sources, the wavelength band between 14.5 and 18 Å is dominated with X-ray line emission from Fe L-shell transitions in Ne-like Fe xvii. The most distinct lines are typically from the $3d \rightarrow 2p$ and $3s \rightarrow 2p$ transitions in Fe xvii at ~ 15 and ~ 17 Å, respectively. Also present in this band is the L-shell emission from Fe xviii, inner-shell satellites from Fe xvi and Fe xv as well as emission from levels with high principal quantum number in O vii and O viii. Many observational, experimental, and theoretical studies of the Fe xvii emission in this band have been completed (see, e.g., Brown 2008 and references therein). These include, for example, measurements of the relative Fe xvii line intensities (Laming et al. 2000; Beiersdorfer et al. 2002, 2004a) as well as measurements of some of the Fe xvii excitation cross sections (Brown et al. 2006) and several theoretical approaches on how to resolve some of the discrepancies noted between the measurements and the modeling calculations (Doron & Behar 2002; Chen & Pradhan 2002; Gu 2003; Fournier & Hansen 2005; Pradhan 2005; Pindzola et al. 2006; Loch et al. 2006; Chen 2008). Moreover, a catalog of the L-shell transitions of Fe xviii through Fe xxiv between 10.6 and 18 Å was established in the laboratory (Brown et al. 2002; Chen et al. 2007) and compared to calculations using many-body perturbation theory (Gu 2005).

The X-ray emission from the relatively weaker inner-shell (IS) satellite transitions in Na-like Fe xvi that fall in this wavelength band have not been as well studied as those from higher charge states even though some features have been suggested to exist in solar flares (Parkinson 1973; Phillips et al. 1982), in the cool corona of Procyon (Raassen et al. 2002) and in laboratory-based spark and laser-induced plasma experiments (Burkhalter et al. 1979). One of the issues behind a long standing debate concerning the line ratio of the $2p_{3/2}^5 3d_{5/2} \ ^3D_1 \rightarrow 2p^6 \ ^1S_0$ (3C) resonance to the $2p_{1/2}^5 3d_{3/2} \ ^1P_1 \rightarrow 2p^6 \ ^1S_0$ (3D) intercombination lines, in Fe xvii can potentially be

explained by line blending from Fe xvi IS satellites. Historically, theoretical calculations of this ratio are higher than terrestrial based experimental values which are then typically higher than values observed in solar and astrophysical plasmas. By comparing calculations to observations from Capella, Behar et al. (2001) found that IS satellites of Fe xvi can enhance the 3D line in Fe xvii by as much as 10%. Further, Brown et al. (2001), using the EBIT-II electron beam ion trap at the Lawrence Livermore National Laboratory (LLNL), showed that an enhancement of 3D by blending with Fe xvi IS satellite lines by up to 50% was possible. This is sufficient to account for the historically low I_{3C}/I_{3D} line ratios observed in solar and stellar coronae when compared to theory and laboratory-based experiments. This effect has subsequently been reinforced by Brickhouse & Schmelz (2006) in their analysis of solar X-ray spectra. The Fe xvi line strengths must therefore be known and taken into account, lest the accuracy of the Fe xvii spectral diagnostics in this wavelength band are compromised.

The Fe xvi IS satellite X-ray spectrum which falls in the wavelength band between 14.5 and 18 Å has been calculated by several authors, including Cornille et al. (1994) and Phillips et al. (1997). Unfortunately, the relative line intensities nor the wavelengths predicted by these calculations agree with each other, which casts doubt on the modeling of the strength, and in principle on the identification of Fe xvi IS satellites, in spectra using theoretical atomic data for Fe xvi.

To provide accurate wavelengths and relative line intensities and to discriminate among different modeling calculations, we have measured the X-ray emission from Na-like Fe xvi under controlled and well-known conditions using the University of California Lawrence Livermore National Laboratory’s EBIT-I electron beam ion trap facility. In our experiments, we confirm the results of Brown et al. (2001) and extend the Fe xvi spectral measurements to longer wavelengths in order to characterize the effects the Fe xvi IS satellites may have on the $3s \rightarrow 2p$ lines of Fe xvii. We present the results of our measurements and compare them with the published theories of Cornille et al. (1994) and Phillips et al. (1997). In addition, we present new

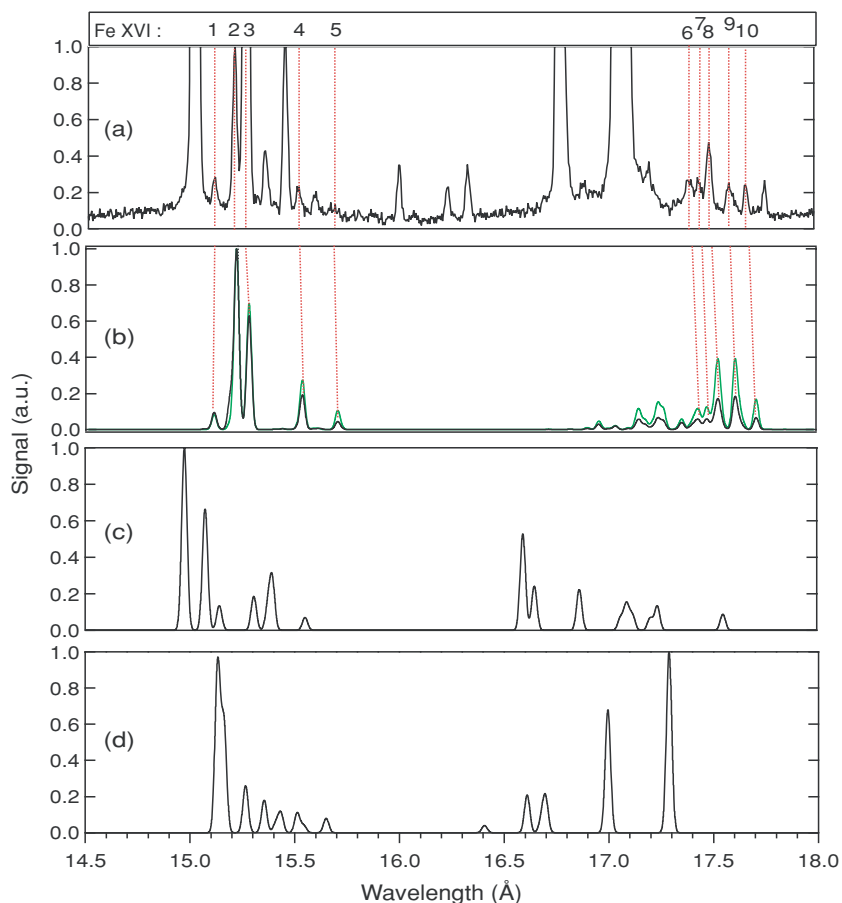


Figure 1. (a) Experimental spectrum at a beam energy of 1.1 keV. Dashed lines indicate the location of the Fe xvi inner-shell satellite features identified in Table 1. The numbers above the top graph refer to the labels used in Table 1. The saturated features belong to well-known transitions in Fe xvii. (b) Theoretical results from FAC for a beam energy of 1.1 keV (black) and 825 eV (green) for a density $n_e = 3 \times 10^{11} \text{ cm}^{-3}$; (c) theoretical results from Cornille et al. (1994) at 816 eV and $n_e < 10^{12} \text{ cm}^{-3}$; (d) theoretical results from Phillips et al. (1997) at 843 eV and $n_e = 10^8 \text{ cm}^{-3}$.

(A color version of this figure is available in the online journal.)

calculation using the Flexible Atomic Code (FAC). This is necessary as we find that the older calculations are difficult to reconcile with the measured spectra.

2. EXPERIMENT

The LLNL EBIT-I electron beam ion trap has been used extensively for laboratory astrophysics (Beiersdorfer 2003, 2008). EBIT-I uses a monoenergetic electron beam to ionize neutral material, excite bound electrons, and trap ions radially. Along the electron beam direction, ions are trapped by different potentials applied to three surrounding drift tubes. The length of the trap along the electron beam is 2 cm. The diameter of the electron beam is $\sim 50 \mu\text{m}$, removing the need for an entrance slit for dispersive spectrometers. A detailed description of the LLNL electron beam ion traps is given by Marrs (1995, 2008).

To observe the spectral emission from the Fe xvi IS satellite lines one must use an electron beam energy greater than $\sim 830 \text{ eV}$. For the measurement presented here, we used an electron beam energy of $1.10 \pm 0.03 \text{ keV}$, which means lines with wavelength as short as 11 \AA can be excited. This energy is well above the 489 eV ionization potential of Fe xvi, and in collisional ionization equilibrium, essentially no Fe xvi ions exist at this beam energy. For our measurement, a relatively large population of Fe xvi ions is sustained by continually introducing iron into the trap in the form of the neutral molecular gas,

iron pentacarbonyl, $\text{Fe}(\text{CO})_5$, with a ballistic gas injector. The continuous injection of neutral iron results in an underionized plasma, and thus a lower ionization state. This is the same method used by Brown et al. (2001).

We employed two spectrometers to observe the X-ray spectrum: a broadband flat crystal spectrometer (Beiersdorfer & Wargelin 1994; Brown et al. 1999) and a flat-field, grazing-incidence reflection grating spectrometer (Beiersdorfer et al. 2004c). The spectrum measured with the grating spectrometer is shown in Figure 1(a). Spectra obtained with the crystal spectrometer are shown in Figures 2 and 3, which are also overlaid with the grating data. The flat crystal spectrometer uses a rubidium acid phthalate (RAP, $2d = 26.121 \text{ \AA}$) crystal for diffraction and a position sensitive proportional counter (PSPC) for detection. The proportional counter uses P-10 gas (90% Ar and 10% CH_4) at a pressure of 760 torr as a detection gas. The crystal spectrometer has $\sim 3 \text{ \AA}$ bandpass and a resolving power of $\lambda/\Delta\lambda \sim 600$ for a wavelength λ in the $14.5\text{--}18 \text{ \AA}$ band. The absorption of X-rays by air in the spectrometer is eliminated by operating at a pressure below 2×10^{-7} torr. This is much higher than the typical pressure in EBIT-I of 10^{-11} torr. To avoid contamination of the vacuum of EBIT-I by the residual gas in the spectrometer, the two chambers are separated by a $0.5 \mu\text{m}$ thick, free-standing polyimide window. Similarly, a $1 \mu\text{m}$ thick polyimide window coated with $\sim 200 \text{ \AA}$ of aluminum and supported by gold coated tungsten wires (Beiersdorfer et al. 2004b) is

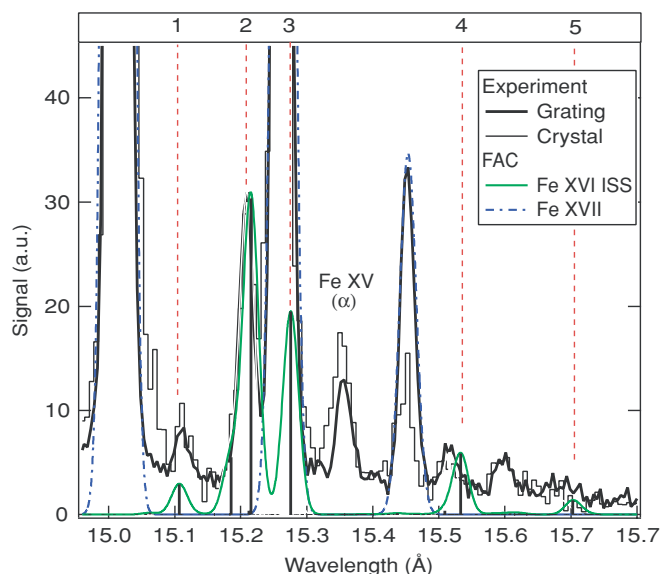


Figure 2. Comparison of results from the crystal spectrometer, the grating spectrometer, and the calculated spectrum from FAC between 15.09 and 15.54 Å. The FAC calculations include emission from Fe XVII and IS satellites from Fe XVI. The spectra are normalized to line 2 at 15.20 Å. The experimental data shown include only broadband corrections to the intensity. There is no correction for polarization effects since they are line specific. The effect of the polarization corrections for most Fe XVI are 10% or less.

(A color version of this figure is available in the online journal.)

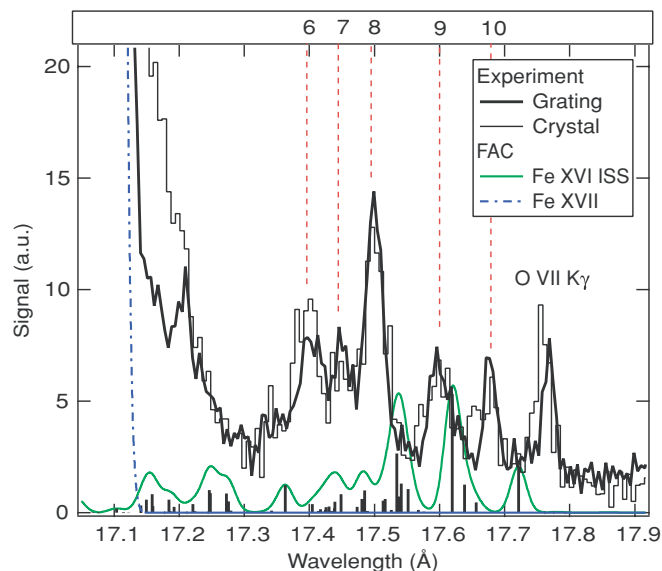


Figure 3. Comparison of experimental data around 17.4 Å from the crystal spectrometer, the grating spectrometer and the calculated spectrum from FAC. The Fe XVI line intensity is normalized to 2 at 15.20 Å. The experimental data shown include only broadband corrections to the intensity, i.e., there is no correction for polarization effects since they are line specific. The effect of the polarization corrections are at most 10%. We also note the contribution from O VII K_{δ} and K_{γ} at 17.396 and 17.768 Å, respectively.

(A color version of this figure is available in the online journal.)

used to isolate the pressure in the PSPC from the vacuum of the spectrometer.

The grating spectrometer uses a variable-line-spacing, gold-coated grating to disperse the spectrum onto a flat field. The average line spacing of the grating is 2400 ℓ/mm and it operates at an incident angle of 2° . X-rays are detected using a two-dimensional back-illuminated charge-coupled detector

(CCD) with a flat instrumental response between 11 and 19 Å (Beiersdorfer et al. 2004c). The bandpass is ~ 7 Å with a resolving power of ~ 600 for λ in the 14.5–18 Å band. The gas load of the spectrometer ($\sim 10^{-7}$ torr) on the EBIT-I vacuum chamber is reduced by a series of baffles between the grating and trap region. No vacuum windows of any kind are used for the grating spectrometer.

2.1. Wavelength Measurement and Line Identification

The wavelength scale of each spectrometer is calibrated using the well-known transition wavelengths of hydrogenic O VIII and helium-like O VII, as well as the Ne-like Fe XVII lines 3C, 3D, 3F, 3G, and M2 measured by Brown et al. (1998). The wavelength of O VIII Ly_{β} was taken from Garcia & Mack (1965). The wavelengths of K_{β} and K_{γ} in O VII are given by Vainshtein & Safranov (1985). These have been adjusted by the more accurate calculation of the O VII $1s^2$ ground state energy by Drake (1988). The injection of CO_2 into the trap allowed the measurement of the oxygen calibration spectra.

For the crystal spectrometer the angle that the crystal makes with the incident radiation from EBIT-I determines the wavelength that is reflected according to Bragg's law,

$$n\lambda = 2d\sin\theta, \quad (1)$$

where n is the order of reflection, d is the crystal lattice spacing, and θ is the Bragg angle. The centroids of each line were fit with a Gaussian function in channel space on the PSPC. A linear regression can then be formed between the centroid channel number and expected Bragg angle allowing the production of a wavelength scale. The wavelength calibration for the grating spectrometer is accomplished in a similar way. In particular, a second-order polynomial fit between known wavelength and channel number is used to establish the wavelength scale. The order of the polynomial was chosen such that the difference between reference wavelengths and those obtained by the calibration is minimized, while ensuring that the distribution of the residuals around zero is random.

The error in the wavelength is taken to be the quadrature sum of the error associated with the calibration scale and that from the fit of the centroid. The error from fitting the centroid includes the statistical contribution from the number of counts in the feature. Since the lines of interest are relatively weak we find that the error from fitting the lines is comparable to the error from establishing the wavelength scale. The largest deviation between known calibration line wavelength values and those inferred from the resulting wavelength scale is 3 mÅ, while the largest error from fitting a weak Fe XVI features is 10 mÅ. The qualitative agreement of the FAC line positions with the measured spectrum has allowed the calculation to be used as a guide for fitting the experimental line shapes. For example, if a line shape seems to be due to a blend of two unresolved Fe XVI IS satellite lines and FAC suggests that there are indeed two or more lines present then a Gaussian with a fixed predetermined width representing a single line, is assigned to each underlying line for the fit. The fit is trusted if the end result fits the data, and the underlying features reflect what FAC predicts is there. This introduces the caveat that if the identified feature is a blend, the wavelength error increases to the maximum separation of the predicted FAC line positions. The largest error in this case is 20 mÅ. The wavelengths of the observed Fe XVI IS satellites inferred from the experiment are given in Table 1 (Column 2).

Table 1
Summary of Wavelengths, Relative Intensities, and Polarizations of the Fe XVI X-ray Lines^a

Label	Wavelength (Å)		Transition	Relative Intensity				Polarization
	Experiment	FAC		Exp ^b	Exp ^c	FAC ^d	FAC ^e	FAC
1 (A) ^f	15.111(4)	15.107	$2p^6 3s J = 1/2 - 2p_{1/2} 2p_{3/2}^4 3s_{1/2} 3d_{5/2} J = 3/2$	0.20(8)	0.22(6)	0.100	0.10	0.22
2a (B) ^f	15.19(2)	15.185	$2p^6 3p_{3/2} J = 3/2 - 2s_{1/2} 2p^6 3s^2 J = 1/2$	0.15(6)	0.16(9)	0.180	0.18	0
2b (B) ^f	15.210(4)	15.215	$2p^6 3s J = 1/2 - 2p_{1/2} 2p_{3/2}^4 3s_{1/2} 3d_{3/2} J = 1/2$	1	1	1	1	0
3 (C) ^f	15.261(3)	15.276	$2p^6 3s J = 1/2 - 2p_{1/2} 2p_{3/2}^4 3s_{1/2} 3d_{5/2} J = 3/2$			0.640	0.64	0.25
4	15.516(5)	15.533	$2p^6 3s J = 1/2 - 2p_{1/2}^2 2p_{3/2}^3 3s_{1/2} 3d_{5/2} J = 3/2$	0.08(7)	0.15(5)	0.190	0.19	0.19
5	15.679(9)	15.703	$2p^6 3s J = 1/2 - 2p_{1/2}^2 2p_{3/2}^3 3s_{1/2} 3d_{3/2} J = 3/2$		0.02(5)	0.040	0.04	-0.19
6a	17.37(1)	17.404	$2p^6 3s J = 1/2 - 2p_{1/2}^2 2p_{3/2}^3 3s^2 J = 3/2$	0.10(4)	0.08(5)	0.010	0.02	-0.28
6b	17.395(4)	17.426	$2p^6 3d_{5/2} J = 5/2 - 2p_{1/2}^2 2p_{3/2}^3 3s_{1/2} 3d_{5/2} J = 5/2$	0.19(5)	0.15(3)	0.010	0.02	-0.28
		17.430	$2p^6 3d_{3/2} J = 3/2 - 2p_{1/2} 2p_{3/2}^4 3p_{3/2}^2 J = 3/2$			0.010		-0.30
6c	17.417(4)	17.439	$2p^6 3d_{5/2} J = 5/2 - 2p_{1/2}^2 2p_{3/2}^3 3s_{1/2} 3d_{5/2} J = 7/2$	0.16(5)	0.12(3)	0.020	0.05	0.15
		17.449	$2p^6 3d_{3/2} J = 3/2 - 2p_{1/2}^2 2p_{3/2}^3 3s_{1/2} 3d_{3/2} J = 3/2$			0.030		-0.07
7	17.447(4)	17.473	$2p^6 3p_{1/2} J = 1/2 - 2p_{1/2}^2 2p_{3/2}^3 3s_{1/2} 3p_{3/2} J = 3/2$	0.17(4)	0.21(3)	0.008	0.06	0.19
		17.481	$2p^6 3d_{3/2} J = 3/2 - 2p_{1/2}^2 2p_{3/2}^3 3s_{1/2} 3d_{3/2} J = 5/2$			0.020		0.07
		17.485	$2p^6 3p_{3/2} J = 3/2 - 2p_{1/2}^2 2p_{3/2}^3 3s_{1/2} 3p_{3/2} J = 1/2$			0.032		0
8a	17.494(6)	17.513	$2p^6 3p_{1/2} J = 1/2 - 2p_{1/2}^2 2p_{3/2}^3 3s_{1/2} 3p_{1/2} J = 1/2$	0.37(6)	0.35(7)	0.017	0.19	0
		17.516	$2p^6 3d_{5/2} J = 5/2 - 2p_{1/2}^2 2p_{3/2}^3 3s_{1/2} 3d_{3/2} J = 7/2$			0.019		0.06
		17.535	$2p^6 3d_{5/2} J = 5/2 - 2p_{1/2}^2 2p_{3/2}^3 3s_{1/2} 3d_{5/2} J = 5/2$			0.087		-0.002
		17.537	$2p^6 3p_{3/2} J = 3/2 - 2p_{1/2}^2 2p_{3/2}^3 3s_{1/2} 3p_{3/2} J = 3/2$			0.024		-0.17
		17.541	$2p^6 3p_{1/2} J = 1/2 - 2p_{1/2}^2 2p_{3/2}^3 3s_{1/2} 3p_{3/2} J = 5/2$			0.043		0.11
8b	17.510(4)	17.552	$2p^6 3p_{1/2} J = 1/2 - 2p_{1/2}^2 2p_{3/2}^3 3s_{1/2} 3p_{1/2} J = 3/2$	0.17(5)	0.24(2)	0.030	0.03	0.04
9a	17.592(4)	17.619	$2p^6 3p_{3/2} J = 3/2 - 2p_{1/2}^2 2p_{3/2}^3 3s_{1/2} 3p_{3/2} J = 7/2$		0.19(3)	0.180	0.18	-0.20
9b	17.612(6)	17.638	$2p^6 3p_{1/2} J = 3/2 - 2p_{1/2}^2 2p_{3/2}^3 3s_{1/2} 3p_{1/2} J = 5/2$		0.11(3)	0.040	0.04	-0.03
9c	17.633(7)	17.656	$2p^6 3p_{1/2} J = 1/2 - 2p_{1/2}^2 2p_{3/2}^3 3s_{1/2} 3p_{1/2} J = 3/2$		0.05(3)	0.020	0.02	0.04
10	17.678(3)	17.721	$2p^6 3p_{3/2} J = 3/2 - 2p_{1/2}^2 2p_{3/2}^3 3s_{1/2} 3p_{1/2} J = 3/2$		0.20(2)	0.070	0.07	-0.03

Notes.

^a Experimental values (Columns 2, 4, and 5) measured with a beam energy of 1.1 keV.

^b Crystal spectrometer results, including corrections from broad band energy dependencies (i.e., foil transmission, crystal reflection) as well as from the anisotropy, polarization, and crystal reflectivity.

^c Grating spectrometer results, including corrections from anisotropy and polarization effects.

^d Individual normalized line intensities.

^e Total line ratio for resolvable feature.

^f The “A”, “B”, and “C” refer to labels used by Brown et al. (2001).

2.2. Relative Line Intensity

A Gaussian line profile fit to each line is used to determine its intensity relative to the strongest line. The width of the Gaussian is determined by an average of widths measured by fitting isolated X-ray lines. This width is instrument specific and determined separately for the grating and crystal spectrometers. After the average is determined, this single value is used in all of the data analysis from the respective instruments. Many of the Fe XVI IS satellites, especially on the long wavelength end of the spectrum are unresolved blends. The spectrum created by FAC is qualitatively similar to the experiment. As mentioned before this similarity guided our choice of the number and wavelength positions of Gaussians used for fitting unresolved line features. The optimum result would be to fit a given blend with the number of features predicted by FAC. This is not always possible when multiple lines are very close. If the fit represents more than one identified feature then the intensity determined from the fit is compared to the sum of the intensities of the lines predicted by FAC. Columns 7 and 8 contain the line ratio results from FAC for the individual features and their total, respectively.

To compare our measured line intensities to theory, the energy dependent response of the spectrometers must be taken into account. For the crystal spectrometer, this includes the transmission efficiency of the foils isolating the spectrometer chamber from EBIT-I, the reflectivity of the crystal, and the absorption efficiency of the detector gas. Using the data on the Center for X-Ray Optics (CXRO) Web site³ for transmission and absorption, broadband intensity corrections have been made to the spectra. Reflectance from the crystal is taken into account by averaging the values given by the Lorentzian and mosaic models provided by Henke et al. (1993) specific to an RAP crystal. There were no absorption edges encountered for any of the materials in question in this region of the spectrum. While the transmission, absorption and reflectance curves were taken from calculation and not measured directly, they have been shown to be in agreement with the values measured previously (Savin et al. 1996). Since the grating spectrometer has a flat instrumental response in the wavelength region under study (Beiersdorfer et al. 2004c), no broadband efficiency

³ <http://www-cxro.lbl.gov/>

corrections were necessary for obtaining accurate normalized line intensities.

In addition to the corrections above, the anisotropy of emitted line radiation produced in an electron beam ion trap must be taken into account. This anisotropy results from the directionality of the beam which can cause a symmetric ($m_{-j} = m_{+j}$) population imbalance of magnetic sublevels leading to a possible linear polarization of the X-ray emission (Beiersdorfer et al. 1996). It can be accounted for by the following:

$$I = \left(\frac{3 - P}{3} \right) I(90^\circ), \quad (2)$$

where P is the polarization of the transition of interest, $I(90^\circ)$ is the line intensity emitted at 90° to the electron beam direction, and I is the total emitted intensity in 4π steradians. This correction is necessary for both spectrometers because they collect light only perpendicular to the beam and not an average over 4π steradian. The form of Equation (2) is specific to electric dipole transitions only and is appropriate for all but one (feature 9a is a magnetic quadrupole transition) of the Fe xvi features identified in this paper. Since the intensity correction for the magnetic quadrupole line cannot be written in a general form it is not shown here.

In the case of the crystal spectrometer, a third additional correction must be included because the crystal acts as a polarimeter preferentially reflecting light polarized perpendicular to the dispersion plane. The relationship between the measured intensity from the crystal spectrometer and the polarization-free, isotropically emitted intensity, can be written as follows (Wargelin 1993),

$$I = \left(\frac{3 - P}{3} \right) \left[\left(\frac{2}{R_{\parallel}} \right) \frac{1}{\left(1 + P + (1 - P) \left(\frac{R_{\perp}}{R_{\parallel}} \right) \right)} \right] I(90^\circ), \quad (3)$$

where R_{\parallel} and R_{\perp} , are the parallel and perpendicular crystal reflectivities given by Henke et al. (1993).

Equations (2) and (3) require knowledge of the polarization for the transitions of interest. The polarizations were calculated using FAC and take into account cascading from levels with principal quantum number $n \leq 4$. The polarizations as calculated by FAC are included in Table 1 (Column 9). A neglected effect in the calculation of the polarization is a depolarization that results from a transverse electron velocity within the beam produced by cyclotron motion of the electrons perpendicular to the magnetic field lines as they travel through the trap (Gu et al. 1999). The polarization changes by up to 20%, but the effect on the line ratios is $< 1\%$.

The measured line intensities, normalized to the Fe xvi line 2b and corrected for spectrometer and polarization effects are given in Table 1 (Columns 5 and 6). The error in the normalized line intensities results from a quadrature sum of the errors from fitting the background and from fitting the line shapes. For the crystal data an extra source of error was included from broadband reflectance and transmission corrections ($\sim 6\%$ of the intensity). Any error introduced from not knowing the exact polarization of specific lines is not taken into account and is deemed to be small. The maximum estimated error is 9%.

3. COMPARISON TO THEORY

In Table 1 our measurements are compared to a simulation based on atomic data computed with FAC version 1.0.9, de-

veloped by Gu (2008).⁴ Specifically, a synthetic spectrum of Fe xvi between 14.5 Å and 18 Å was calculated. For a monoenergetic electron beam with an energy of 1.1 keV, electron impact excitation followed by radiative cascades, as well as autoionization into the ground state of Ne-like Fe xvii, are the processes that determine the strengths of the Fe xvi X-ray lines in this band. Since the beam energy is well above any threshold for dielectronic recombination of Fe xvii for the region of interest, the Fe xvi spectrum is comprised of solely inner-shell satellites. The atomic structure and line formation calculations by FAC are fully relativistic and use the distorted wave approximation for interaction with continuum states. Autoionization of Fe xvi from $2s2p^63l^2$, $2p^53l^2$, $2s2p^63l4l'$, and $2p^53l4l'$ with l and $l' = 0, 1, 2$ into the ground state of Fe xvii is included. These model calculations create 242 energy levels which result in nearly 30,000 transitions. When the synthetic spectrum is broadened to simulate the data, 10 Fe xvi features with a relative intensity greater than 0.02 are found in the 14.5–18 Å bandwidth. The transitions that have a relative intensity greater than 0.01 and are responsible for these features are listed in Table 1 (Column 7). The wavelengths predicted by FAC were typically long by as much as 50 mÅ, the largest deviation being at the longest wavelength.

We note that line 9a is identified as a magnetic quadrupole transition, $(2p_{3/2}^5 3s_{1/2} 3p_{3/2})_{(J=7/2)} \rightarrow (2p^6 3p_{3/2})_{(J=3/2)}$. Normally, forbidden inner-shell transitions are rarely observed, because of the large autoionization rate of their upper levels that reduces the radiative yield. However, in this particular case, the $(2p_{3/2}^5 3s_{1/2} 3p_{3/2})_{(J=7/2)}$ level has a very small autoionization rate of $3.6 \times 10^4 \text{ s}^{-1}$, while the magnetic quadrupole transition rate is calculated to be $1.7 \times 10^5 \text{ s}^{-1}$, making this line an observable feature.

For comparison to other calculations, we also include in Figure 1 predictions of the Fe xvi IS satellites from Cornille et al. (1994) and from Phillips et al. (1997) under similar conditions. Cornille used SUPERSTRUCTURE (Eisner et al. 1974) to calculate the energy levels and radiative transition rates along with DISWAV (Eisner et al. 1972), JAJOM (Saraph 1972) and JJOMCBE to calculate collision strengths. The autoionization rates come from the code AUTOLSJ (Dubau & Louergue 1981). The Fe xvi configurations included in the calculation are $2p^6 3s$, $2p^5 3s^2$, $2p^5 3s 3p$, and $2p^5 3s 3d$, making a total of 44 levels and resulting in ~ 12 – 15 resolvable features. The line emissivities were determined for an electron impact energy of 816 eV (60 Ry) at an electron density $< 10^{12} \text{ cm}^{-3}$. Phillips et al. (1997) used the same computational scenario except that the collision strengths were calculated using DSTWAV (Burke & Eisner 1983) at an electron temperature of 843 eV (62 Ry) and a density of 10^8 cm^{-3} . The predicted wavelengths roughly match those given by the relativistically corrected Hartree–Fock code written by Cowan (1981) and used by Phillips et al. (1997).

Comparing the predictions of Cornille et al. (1994) and Phillips et al. (1997) with our measurements we note that there is a dramatic difference both for the predicted relative intensity and line position. Most importantly both calculations predict strong, well-resolved lines near 17 Å. In particular, Cornille et al. (1994) predict well-resolved lines at 16.6 and 16.7 Å; Phillips et al. (1997) predict strong lines at 17.0 and 17.3 Å. These lines would serve as a diagnostic for the Fe xvi abundance

⁴ <http://sprg.ssl.berkeley.edu/~mfgu/fac>

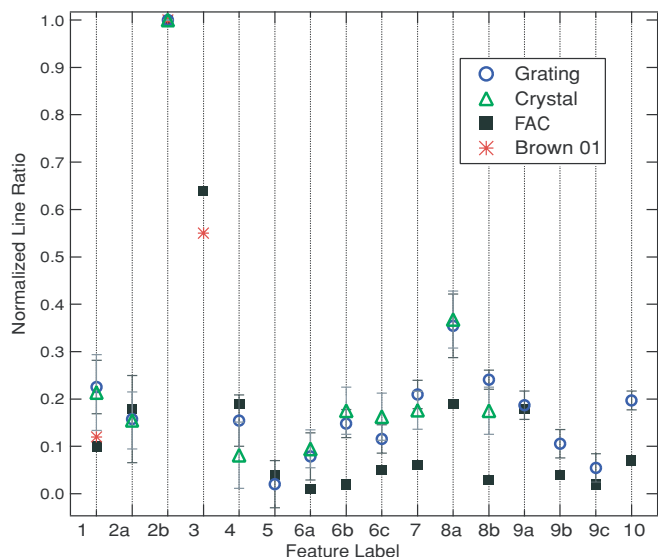


Figure 4. Line intensities of Fe xvii IS satellites relative to line 2 at 15.20 Å. The squares are taken from the calculated spectrum produced by FAC. The triangles are from the crystal spectrometer. The circles are from the grating spectrometer. The stars are from Brown et al. (2001). The feature labels refer to those in Table 1.

(A color version of this figure is available in the online journal.)

in the plasma, if the lines were indeed as strong as predicted. Our measurements and FAC calculations show that these lines are neither at these positions nor strong.

Finally, we make a comparison between the calculated relative intensities from FAC and those from experiment for a few of the larger Fe xvii features (Figure 4). The experimental data from the grating and crystal spectrometers tend to agree to within 10%. Unfortunately there are five features from the crystal data which could not be fit properly because of line blending and poor statistics. There is agreement to within a factor of 2 between FAC and experiment for features 2a, 4, 5, and 9a. Otherwise the results from FAC tend to be smaller by a factor of at most 7. It should be noted that the FAC results calculated for a lower beam energy progressively enhanced the longer wavelength features until the ionization threshold was reached. The lower values of the long wavelength line intensities from FAC could be attributed to the difficulty in calculating accurate branching ratios when including the $3s$, $3p$, and $3d$ family of energy levels. The full reason for the predominantly lower results from FAC is unknown. Despite this difference the qualitative agreement with experiment is quite good. There is also a quantitative agreement between our results and the independent calculation and measurement of Brown et al. (2001) represented by the stars in Figure 4. The predicted value of feature 3 is a factor of ~ 1.1 higher than our result. This small difference is probably because the blend of feature 2 (i.e., the blending of lines 2a and 2b) was not accounted for in Brown et al. (2001). Treating 2a and 2b as a single line increases its area and thus decreases the relative line strength of feature 4. It should be noted that blending of K_{δ} from O vii with feature 6a and 6b at ~ 17.38 Å has been taken into account for both the grating and crystal data. In each case the oxygen spectrum is normalized to K_{γ} . The spread in the data combined with the results from FAC show the normalized line intensities presented here to be good to within 20%.

4. CONCLUSION

We have used the EBIT-I electron beam ion trap with high resolution crystal and grating spectrometers to measure the wavelengths and normalized line intensities of some of the larger inner-shell satellites from Fe xvii between 14.5 and 18 Å. The Fe xvii lines have been found to be important contributors to the L-shell iron spectrum. Line ratio diagnostics using features from Fe xvii need to account for blending with the Fe xvii IS satellites, depending on the spectral resolution of the instrument and the charge state distribution of the source. Fe xvii lines 3C and 3F do not blend with Fe xvii lines. Lines M2 and 3G may blend in a minor way ($\leq 2\%$), while the contribution of Fe xvii lines to the Fe xvii line 3D can be strong.

The predictions of the relatively strong lines by Phillips et al. (1997) and by Cornille et al. (1994) between 16.5 Å and 17 Å are not confirmed by our measurements. These lines should, thus, not be used as indicators of the presence of Fe xvii IS satellite line emission. Instead, the strongest unblended indicator is the 15.20 Å line, feature 2b in Table 1, which is located on the short-wavelength side of line 3D.

We find a qualitative agreement between our measurement and the synthetic spectrum from FAC. The wavelengths deduced from FAC are slightly long and with a difference that increases with wavelength to a maximum of 50 mÅ. The line ratios for features 2a, 4, 5, and 9a show a quantitatively good agreement with experiment. Otherwise the line ratio results from FAC tend to be lower by factor of at most 7. The predicted line ratio of feature 3 at 15.26 Å, which invariably blends with line 3D from Fe xvii, is in agreement with the value predicted in Brown et al. (2001).

The work at Lawrence Livermore National Laboratory was performed under the auspices of the Department of Energy under Contract W-7405-ENG-48 and supported by the Astronomy and Physics Research and Analysis Program of the National Aeronautics and Space Administration (NASA) under contract NNG06WF08I.

REFERENCES

- Behar, E., Cottam, J., & Kahn, S. 2001, *ApJ*, **548**, 966
 Beiersdorfer, P. 2003, *ARA&A*, **412**, 343
 Beiersdorfer, P. 2008, *Can. J. Phys.*, **86**, 1
 Beiersdorfer, P., Bitter, M., von Goeler, S., & Hill, K. W. 2004a, *ApJ*, **610**, 616
 Beiersdorfer, P., Brown, G. V., Goddard, R., & Wargelin, B. J. 2004b, *Rev. Sci. Instrum.*, **75**, 10, 3720
 Beiersdorfer, P., Magee, E. W., Träbert, E., Chen, H., Lepson, J. K., Gu, M.-F., & Schmidt, M. 2004c, *Rev. Sci. Instrum.*, **75**, 10, 3723
 Beiersdorfer, P., & Wargelin, B. J. 1994, *Rev. Sci. Instrum.*, **65**, 13
 Beiersdorfer, P., et al. 1996, *Phys. Rev. A*, **53**, 3974
 Beiersdorfer, P., et al. 2002, *ApJ*, **576**, L169
 Brickhouse, N. S., & Schmelz, J. T. 2006, *ApJ*, **636**, L53
 Brown, G. V. 2008, *Can. J. Phys.*, **86**, 199
 Brown, G. V., Beiersdorfer, P., Chen, H., Chen, M. H., & Reed, K. J. 2001, *ApJ*, **557**, L75
 Brown, G. V., Beiersdorfer, P., Liedahl, D. A., Widmann, K., & Kahn, S. M. 1998, *ApJ*, **502**, 1015
 Brown, G. V., Beiersdorfer, P., Liedahl, D. A., Widman, K., Kahn, S. M., & Clothiaux, E. J. 2002, *ApJS*, **140**, 589
 Brown, G. V., Beiersdorfer, P., & Widmann, K. 1999, *Rev. Sci. Instrum.*, **70**, 1, 280
 Brown, G. V., et al. 2006, *Phys. Rev. Lett.*, **96**, 253201
 Burke, P. G., & Eisner, W. 1983, *Atoms in Astrophysics* (New York: Plenum Press)
 Burkharter, P. G., Cohen, L., Cowan, R. D., & Feldman, U. 1979, *J. Opt. Soc. Am.*, **69**, 1133
 Chen, G. X. 2008, *MNRAS*, **386**, L62

- Chen, H., Gu, M. F., Behar, E., Brown, G. V., Kahn, S. M., & Beiersdorfer, P. 2007, *ApJS*, **168**, 319
- Chen, G. X., & Pradhan, A. K. 2002, *Phys. Rev. Lett.*, **89**, 013202
- Cornille, M., Dubau, J., Faucher, P., Bely-Dubau, F., & Blancard, C. 1994, *A&A Suppl. Ser.*, **105**, 77
- Cowan, R. D. 1981, *The Theory of Atomic Structure and Spectra* (Berkeley: Univ. Colorado Press)
- Doron, R., & Behar, E. 2002, *ApJ*, **574**, 518
- Drake, G. W. 1988, *Can. J. Phys.*, **66**, 586
- Dubau, J., & Loulergue, M. 1981, *Phys. Scr.*, **23**, 136
- Eisner, W., Jones, M., & Nussbaumer, H. 1974, *Comp. Phys.*, **8**, 270
- Eisner, W., & Seaton, M. J. 1972, *J. Phys. B*, **5**, 2187
- Fournier, K. B., & Hansen, S. B. 2005, *Phys. Rev. A*, **71**, 012717
- Garcia, J. D., & Mack, J. E. 1965, *J. Opt. Soc. Am.*, **55**, 6, 654
- Gu, M. F. 2003, *ApJ*, **582**, 1241
- Gu, M. F. 2005, *ApJS*, **156**, 105
- Gu, M. F. 2008, *Can. J. Phys.*, **86**, 675
- Gu, M. F., Beiersdorfer, P., & Savin, D. W. 1999, *J. Phys. B*, **32**, 5371
- Henke, B. L., Gullikson, E. M., & Davis, J. C. 1993, *At. Data Nucl. Data Tables*, **54**, 335
- Laming, J. M., et al. 2000, *ApJ*, **545**, L161
- Loch, S. D., Pindzola, M. S., Ballance, C. P., & Griffin, D. C. 2006, *J. Phys. B*, **39**, 85
- Marrs, R. E. 2008, *Can. J. Phys.*, **86**, 11
- Marrs, R. E. 1995, *Experimental Methods in the Physical Science, Atomic Molecular and Optical Physics: Charged Particles*, Vol. 29a (San Diego: Academic Press), 391
- Parkinson, J. H. 1973, *A&A*, **24**, 215
- Phillips, K. J. H., et al. 1982, *ApJ*, **256**, 774
- Phillips, K. J. H., Greer, C. J., Bhatia, A. K., Coffey, I. H., Barnsley, R., & Keenan, F. P. 1997, *A&A*, **324**, 381
- Pindzola, M. S., Loch, S. D., Ballance, C. P., & Griffin, D. C. 2006, *Phys. Rev. A*, **73**, 012718
- Pradhan, A. K. 2005, in *X-Ray Diagnostics of Astrophysical Plasmas: Theory, Experiment, and Observation*, CP774, ed. R. Smith (New York: AIP), **119**
- Raassen, A. J. J., et al. 2002, *A&A*, **389**, 228
- Saraph, H. E. 1972, *Comput. Phys. Comm.*, **3**, 256
- Savin, D. W., Beiersdorfer, P., López-Urritia, Decaux, V., Gullikson, E. M., Kahn, S. M., Liedahl, D. A., Reed, K. J., & Widmann, K. 1996, *ApJ*, **470**, 73
- Vainshtein, L. A., & Safranov, U. I. 1985, *Phys. Scr.*, **31**, 519
- Wargelin, B. J. 1993, PhD Thesis